ACS Combinatorial Science

RESEARCH ARTICLE

pubs.acs.org/acscombsci

Fluorescence-Based High Throughput Screening for Noble Metal-Free and Platinum-Poor Anode Catalysts for the Direct Methanol Fuel Cell

F. G. Welsch, K. Stöwe, and W. F. Maier*

Lehrstuhl für Technische Chemie, Universität des Saarlandes, Gebäude C4 2, 66123 Saarbrücken, Germany

Supporting Information

ABSTRACT: We describe here the results of a high throughput screening study for direct methanol fuel cell (DMFC) anode catalysts consisting of new elemental combinations with an optical high-throughput screening method, which allows the quantitative evaluation of the electrochemical activity of catalysts. The method is based on the fluorescence of protonated quinine generated during electrooxidation of methanol. The high-throughput screening included noble-metal free binary and ternary mixed oxides of the elements Al, Co, Cr, Cu, Fe, Mn, Mo, Nb, Ni, Ta, Ti, Zn, and Zr in the oxidized form as well as after prior reduction in hydrogen. In addition 318 ternary and quaternary Pt-containing materials composed out of the mixed oxides of Bi, Ce, Co, Cr, Cu, Fe, Ga, Ge, In, La, Mn, Mo, Nb, Nd, Ni, Pr, Sb, Sn, Ta, Te, Ti, V, Zn, and Zr with a molar Pt-ratio of 10% and 30% were screened. Validation and long time experiments of the hits were performed by cyclovoltammetry (CV). The microstructural stability of the electrode preparations of the lead compositions was studied by X-ray diffraction (XRD) pattern analysis.

KEYWORDS: DMFC, anode catalyst, high throughput screening, noble-metal free, fluorescence screening

1. INTRODUCTION

Compared to other types of fuel cells the direct methanol fuel cell (DMFC) reveals several advantages for a decentralized power supply: operating at low temperatures and with the possibility to design compact membrane electrode assemblies (MEAs) the main advantages of DMFC lie in the high power density of methanol compared to hydrogen with an electron number ratio per mole feed of $n_e(CH_3OH):n_e(H_2) = 3:1$, its ease of transport, and the lack of a reforming stage to generate the feed from fossil resources. This makes the DMFC applicable for a variety of technical areas, especially mobile devices such as mobile phones, PDAs, laptops, or even for electric vehicles. In addition, the compatibility of methanol with the existing petrol distributions system may become a key aspect for potential future applications of the DMFC. Methanol as well as Fischer–Tropsch products can also be produced from synthesis gas, which can be derived from biomass feedstocks.

On the other side several challenging technical issues have to be met in DMFCs: Nafion with a high density of sulfonic groups[1] used as electrolyte in DMFCs determines the acidic milieu of the catalyst/polymer membrane interface (pH ∼ 1). Therefore, the corrosion resistance of the electrocatalysts is an absolute prerequisite narrowing the compositional space drastically. Platinum has shown the best activity for the electrooxidation of methanol at temperatures below 80 °C.[2,3] CO, formed during electrooxidation of methanol, is well-known to poison platinum. Adsorbed CO is removed by hydroxyl groups (OH) formed through water activation on the platinum surface. Such water activation is responsible for a high overpotential for the electrooxidation of methanol on platinum.[4] Alloying Platinum with oxophilic metals, such as Ruthenium, decreases the overpotential because of the water activation. The binary platinum–ruthenium (PtRu) alloy shows the best activity for the electrooxidation of methanol.[4] Still, methanol oxidation kinetics is slowed down, since ruthenium does not adequately activate water in the electrooxidation of methanol.[5]

The present economic weakness of the DMFC as a decentralized mobile power source is associated with the high noble-metal contents of the Pt-cathode and the PtRu-anode in combination with the slow reaction kinetics of electrode reactions.[6] Because of the lack of alternative catalyst systems, global research activity concentrates on improvements of the PtRu catalyst system and reduction of the noble metal content,[7−9] as well as on the search for new or alternative noble metal containing elemental compositions of anode catalysts[10] and noble metal free catalyst, NiZr,[11] NiTi, transition metal oxides, and W-based systems.[12]

To accelerate the discovery of new elemental DMFC anode catalyst compositions and the process of catalyst optimization several high-throughput (HT) methods have been published. These HT methods can be divided into two groups based on the screen used for the detection of active materials. The first group is based on the parallel measurement of current or potential variations during the electrooxidation of methanol.[13−15] One

Received: May 26, 2011
Revised: August 7, 2011
Published: August 10, 2011

limiting factor for the array size and therefore the size of the materials library is the complex and costly hardware needed.[16] In contrast to this group, high-throughput setups based on the detection of optical effects induced by consecutive reactions of the protons produced during the methanol conversion are attractive alternatives with respect to hardware complexity and cost. In 1998 Smotkín, Mallouk, and coworkers published a HT method, which allowed qualitative differentiation of noble-metal alloys with respect to their electrochemical activity for methanol oxidation by an optical method.[17] On the basis of the transformation of quinine (at neutral pH) and the Ni^{2+} complex of 3-pyridin-2yl-[4,5,6]triazolo[1,5-*a*]pyridine (at low pH) into a protonated, fluorescent-active form during the drop of the pH resulting from methanol conversion, the optimum compositions of quaternary alloys have been identified successfully. Mapping of active regions on a working electrode array and optimization of catalyst compositions have been reported by such fluorescence experiments.[18−20] The charm of such a method is its simplicity. In a comparison of high-throughput electrochemical methods for DMFC anode catalyst development the optical screening method was identified as effective for ranking by high and low activity and for surveys with large numbers of materials.[5] The major drawback of such simple fluorescence experiments is the lack of quantification, since it provides only yes/no answers. In 2007 Jin et al.[21] followed by Gregoire et al.[22] published the first semi-quantitative observation of the fluorescence development during a potential sweep.

In this work, we present the high-throughput screening results of the first combination of the versatile sol−gel process with respect to automation and elemental compositions of the achieved materials[23] with a fast parallel and quantitative optical screening method for DMFC catalysts as published before.[10] We concentrated our study on noble-metal free compounds and on ternary and quarternary compounds with low Pt metal content.

2. MATERIALS AND METHODS

Notation and Synthesis of Compounds. A simplified notation is used to name the examined materials: the composition of a binary mixed oxide (O_x) is generally described as $A_aB_bO_x$. A and B denote a particular element, the lower case a and b describe the molar fraction of the respective element in mol % (with a + *b* = 100 mol %) not accounting for the oxidation states of the elements in the compound and thus not for any oxide content, since this may vary depending on treatments and environment. Consequently, the mixture may be either metallic or oxidic or a mixture of both. Only materials processed before reduction with H_2 also contain the O_x, indicating a true oxide without precise information on the oxidation states. The material obtained out of the reduction of the same mixed oxide with H_2 was denoted as A_aB_b.

Materials were synthesized by a modified sol−gel process as described previously.[24−26] Synthesis was planned and controlled by the software Plattenbau[27] and carried out with the help of a pipetting robot (Zinsser Lissy). The stock solutions were prepared with a 0.25 or 0.1 M precursor dissolved in a mixture of isopropanol (Sigma-Aldrich) and propionic acid (Sigma-Aldrich) with a ratio of 1:1 (v/v). Precursors and concentrations used are specified in Table 1. The stock solutions were mixed in 1.5 mL GC vials according to the ratios of the elements in the favored compound. After mixing, the samples were placed in an orbital shaker (Titramax 100, Heidolph) for 1 h, dried for 2 days at room temperature and for additional 8 days at 40 °C. The mixed oxides were obtained after calcination of the gels under static air at 250 and 400 °C, respectively, for 5 h (heating rate 30 °C/h). After calcination, a part of the samples were reduced under pure hydrogen in an oven with gas supply (VMK-80-Vac, Linn High-therm, 50 mL/min) at 450 °C for 1 h (heating rate 13 °C/min).

Table 1. Precursors, Suppliers, and Concentrations of the Prepared Stock Solutions

precursor[a]	concentration[b] [mol L^{-1}]	supplier
$Bi(ac)_3$	0.25	Sigma-Aldrich
$Co(ac)_2 \cdot 4\ H_2O$	0.25	Lancester
$Ce(acac)_3$	0.25	ABCR
$[Cr\ (ac)_2 \cdot H_2O]_2$	0.25	Sigma-Aldrich
$Cu(ac)_2$	0.25	Johnson Mathey
$Fe(ac)_2$	0.25	Sigma-Aldrich
$Ga(acac)_3$	0.25	ABCR
$Ge[OCH(CH_3)_2]_3$	0.25	Sigma-Aldrich
$In(acac)_3$	0.25	ABCR
$La(acac)_2$	0.25	Sigma-Aldrich
$Mn(acac)_2$	0.25	Sigma-Aldrich
$Mo_2(ac)_4$	0.25	Sigma-Aldrich
$Nb(OCH_2CH_3)_5$	0.25	ABCR
$Nd(ac)_3$	0.25	Sigma-Aldrich
$Ni(ac)_2 \cdot 4\ H_2O$	0.25	Alfa Aesar
$Pr(ac)_3 \cdot 3\ H_2O$	0.25	Sigma-Aldrich
$[(NH_3)_4Pt](ac)_2$	0.25	Umicore
$Ru(acac)_3$	0.10	Sigma-Aldrich
$Sb[OCH(CH_3)_2]_3$	0.25	Alfa Aesar
$Sn[ac]_4$	0.25	Sigma-Aldrich
$Ta(OC_2H_5)_5$	0.25	ABCR
$Te[OCH(CH_3)_2]_4$	0.25	ABCR
$Ti[OCH(CH_3)_2]_4$	0.25	Alfa Aesar
$VO[OCH(CH_3)_2]_3$	0.25	Sigma-Aldrich
$Y[OCH(CH_3)_2]_3$	0.25	Lancester
$Zn(ac)_2$	0.25	Alfa Aesar
$Zr(OCH_2CH_2CH_3)_4$	0.25	Sigma-Aldrich

[a] ac: acetate, acac: acetylacetonate. [b] Metal in *i*-propanol/propionic acid (1:1, v/v).

Fluorescence Based Measurements. All fluorescence based measurements were performed in the setup described before (Figure 1 shows the equipmental setup and the graphite library).[10] The base electrolyte solution was composed of 100 μM quinine (Fluka) and 0.1 M sodium sulfate (Sigma-Aldrich) in water. Determination of the methanol oxidation activity was performed in an electrolyte containing 1 M methanol in water. All experiments were performed in deionized water (Elga Purelab UVF, Elga Labwater). The fluorescence emission resulted from irradiation by an UV lamp at 365 nm (VL-115 L, 15 W, UV Consulting Peschl). A platinum net was used as counter electrode and a $Hg/HgSO_4$ electrode (ref 621, Radiometer Analytical) as reference electrode. A self-made salt bridge unit[10] was used for the connection of the counter electrode region and the reference electrode region on the working electrode array. All potentials were obtained versus the standard hydrogen electrode (SHE). A potentiostat (PP 220, Zahner Elektronik) was used to control the potential of the working electrode array between 0 and 1.175 V versus SHE. For the fluorescence based validation

dx.doi.org/10.1021/co2000967 |*ACS Comb. Sci.* 2011, 13, 518–529

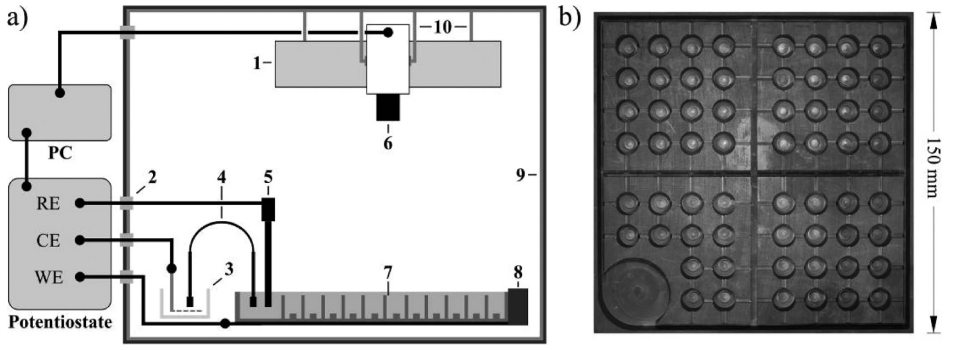

Figure 1. (a): Equipment setup: 1, UV-lamp; 2, light-tight feed throughs; 3, beaker for working electrode (AE) and counter electrode (GE); 4, tubular salt bridges; 5, reference electrode (RE); 6, CCD-camera; 7, working electrode array; 8, positioning device; 9, light tight wooden box; 10, holders for lamp and camera. (b) Top view of graphite library (working electrode array).

experiments tailor-made frits[10] were positioned in the channels next to the coated material spots to increase the data quality.

Coating of Working Electrode Spots. For the coating of the electrode spots, 5 ± 0.15 mg of the catalysts were dispersed for 10 min in a mixture of ethylene glycol and water (7:3 (v/v), mass concentration 0.35 mg/30 μL) using an ultrasonic bath (MK 100, Bandelin). Thirty microliters of the catalyst dispersion were pipetted directly from the dispersion vial positioned in the ultrasonic bath to the catalyst support area on the working electrode array. The removal of the ethylene glycol water mixture was carried out in a vacuum oven at room temperature for 1 h at 0.2 bar followed by 16 h at $\sim 10^{-3}$ mbar.

After drying of the catalyst coatings, 10 μL of a 0.05% Nafion solution in isopropanol (Standard: Nafion 117 solution, 5%; Sigma-Aldrich) was pipetted on top of each of the catalyst coatings and dried for 20 min in an argon flow. The achieved coatings were rinsed with water for 5 h by filling the wells of the working electrode with 500 μL of deionized water to allow the Nafion to reach its swelling state. Before the measurement, the water was removed by the use of a water-driven pump.

Automated Data Acquisition, Processing, and Analysis. Images were acquired and processed automatically using a PC and commercial imaging software (Image Pro Plus, Media Cybernetics). The potentiostat was controlled by a tailor-made Labview application. Images were obtained after a holding time of 1 min at potentials between 300 mV and 1000 mV in steps of 10 mV and between the 1000 mV and 1175 mV versus SHE in steps of 25 mV. Additionally, an image for background subtraction was acquired at the beginning of the measurement. Using Image-Pro Plus software, 60 areas of interests (AOI) in each image were defined according to well positions. A bitmap analysis for each AOI was carried out. The summation of the gray scale values obtained for each pixel was realized using a commercially available spreadsheet calculation software, resulting in intensity values with arbitrary units for each well and potential, respectively. For data analysis, the intensity values were plotted against the potential versus SHE. The automation of data analysis was achieved by the use of a macro software tool (MacroTools Works, Pitrinec Inc.).

Cyclovoltammetry (CV). For validation of hits from the optical screening, standard CV measurements were applied. The CV experiments were carried out at 25 °C in a three-electrode cell connected with the potentiostat specified above controlled with the software PP Inspector (Zahner Elektronik). An oxygen-free (purged with argon) 0.5 M H_2SO_4 solution containing 1 M methanol was used as electrolyte for methanol oxidation experiments (20 cycles). Pretreatment of the electrode preparation was achieved by cycling in an oxygen-free 0.5 M H_2SO_4 solution (10 cycles). The anodes for the activity validations were prepared as described above on glassy carbon sticks (5 mm in diameter, 50 mm in length, Sigradur G, HTW GmbH). For stability testing, the coatings were prepared by pipetting 200 μL of a catalyst dispersion in a mixture of ethylene glycol and water (7:3 (v/v), mass concentration: 3.0 mg/200 μL)) prepared as described above on glassy carbon plates (15 mm in diameter, 2 mm in height, Sigradur G, HTW GmbH). The sticks and the plates were mounted in a tailor-made Teflon holder containing a gold tip as current collector. Before measurement the achieved coatings were rinsed by pipetting 30 μL or 200 μL of deionized water respectively on the coating surface. Before the measurement, the water was removed by the use of a lint-free cloth. A Pt wire was used as counter electrode. The measurements were carried out between 0 V and 1.050 V versus SHE with a scan rate of 20 mV/s.

X-ray Diffraction (XRD) Measurements. XRD measurements of the noble-metal free mixed oxides was performed with powdered materials on a Guinier camera G670 (Huber) with $Cu_{K\alpha 1}$ radiation (λ = 0.154056 nm). The powders were placed on an amorphous polymer tape. The XRD measurement of Pt containing materials was performed on a X'Pert Pro system (PANalytical) with a $\theta-\theta$ geometry using Ni-filtered Cu radiation ($Cu_{K\alpha 1}$ and $Cu_{K\alpha 2}$, λ = 0.154060 and 0.154443 nm, respectively). Diffraction patterns were obtained before and after the CV measurements on glassy carbon plates.

3. RESULTS AND DISCUSSION

Fluorescence-Based High Throughput Screening. The high-throughput technology developed earlier and used here allows the mapping of fluorescence intensity against applied potential. As shown in Figure 2 for the PtRu reference catalyst, the signal obtained correlates very well with the standard CV curve. Therefore, it became possible to use this optical method for screening of the electrochemical performance of potential anode electrocatalysts for DFMC.

Definition of Comparative Parameters of the Materials' Activity for the Electrooxidation of Methanol. The definition of comparative parameters is the basic step concerning a mapping of the materials' activity for the reaction of interest. As published before[10] the fluorescence onset potential E_{Onset} was used for validation of the developed high-throughput method.

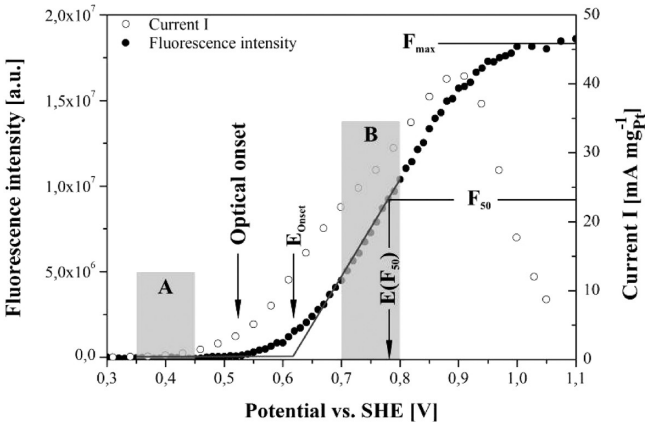

Figure 2. Comparison of fluorescence intensity and the current of PtRu (0,35 mg) measured during the methanol oxidation. Comparative values of the materials' activity toward the electrooxidation of methanol; E_{Onset}, fluorescence onset potential; F_{max}, maximum fluorescence intensity; F_{50}, half fluorescence intensity; $E(F_{50})$, half fluorescence potential. The methanol oxidation current was measured in 0.5 M H_2SO_4 solution.

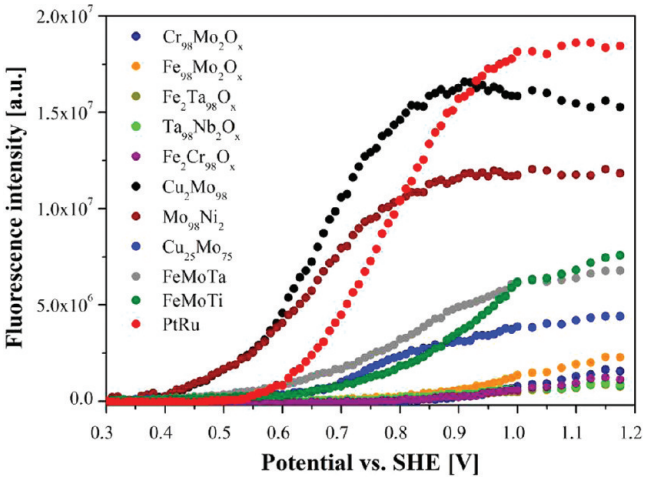

Figure 3. Increase of the fluorescence intensity during the potential sweep in the high-throughput screening over noble metal-free electrodes.

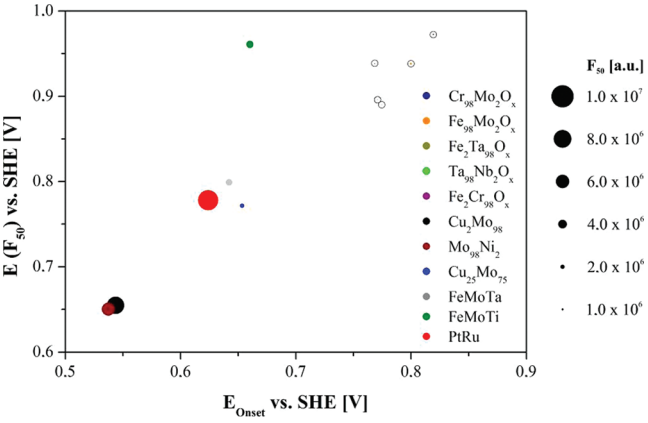

Figure 4. Comparison of the noble-metal free materials activity toward the electrooxidation of methanol obtained in the high-throughput screening by means of their position in the $E(F_{50})/E_{Onset}$ plane and the fluorescence intensity F_{50}, annular marks: materials with an F_{50} value smaller than 1.0×10^6 a. u.

Calculated as the interception point of the two regression lines obtained from the regression analysis of the two data ranges A and B given in Figure 2, a low fluorescence onset potential value E_{Onset} was defined as the main indicator for a high activity of the investigated compounds. Additionally, the half-fluorescence potential $E(F_{50})$, obtained as the potential value according to the fluorescence intensity half of the maximum fluorescence intensity F_{max}, was introduced as comparative value. By plotting $E(F_{50})$ versus E_{Onset} including the half-fluorescence intensity F_{50} indicated by the dot size, a useful visualization of the activity of the materials could be obtained (e.g., Figure 4). Materials with a higher methanol conversion are located in the bottom left corner and materials with a lower methanol conversion are located in the upper right corner in the $E(F_{50})/E_{Onset}$ versus SHE [V] plane on condition that they show a comparable F_{50} value.

High-Throughput Screening of Noble-Metal Free Materials. In a first attempt toward the screening of 550 binary and ternary mixed oxides including the elements Al, Co, Cr, Cu, Fe, Mn, Mo, Nb, Ni, Ta, Ti, Zn, and Zr with the elemental compositions $A_aB_bO_x$ with a = 2, 10, 25, 75, 90, 98 mol % and $b = (100 - a)$ and $A_aB_aC_aO_x$ with a = 33.3 mol %, respectively, were synthesized by the sol−gel process. To extend on the one hand the number of materials and on the other hand enlarge the materials characteristics from mixed oxides toward partially or fully reduced materials, a part of each mixed oxide was reduced in a hydrogen flow (0th generation) resulting in another set of 550 materials, now partly reduced. Because of the paramount importance of the stability of a catalyst in the acidic environment of a fuel cell MEA with a pH of ∼1, the 1100 materials were screened for their acid stability by the fast optical prescreening described before.[10] The preselection of unsuitable materials before the electrochemical evaluation thus accelerated the electrochemical screening process. From the 1100 materials only 260 materials were identified as acid stable toward 1 M H_2SO_4 over a time period of up to 72 h (1st generation). In the fluorescence-based screening of the materials' activity toward the electrooxidation of methanol, only 10 materials showed an increase in the fluorescence intensity at the applied potential range between 0.300 and 1.175 V versus SHE (see Figure 3). All 10 materials have been reduced under hydrogen prior to the study, so none of the unreduced mixed oxides showed significant electrocatalytic activity. Cu_2Mo_{98} and Ni_2Mo_{98} showed E_{Onset} values and therefore $E(F_{50})$ values lower than PtRu. For Cu_2Mo_{98} a comparable F_{50} value was detected indicative of comparable total activity. Because of comparable $E(F_{50})$ and E_{Onset} values $Cu_{25}Mo_{75}$ and FeMoTa are situated next to PtRu in the $E(F_{50})/E_{Onset}$ versus SHE [V] plane but a lower fluorescence development during the measurement led to lower F_{50} values. In the case of FeMoTi a low E_{Onset} value and a high $E(F_{50})$ value led to a distant position relative to the PtRu area and a smaller F_{50} value caused by a minor fluorescence development. All other mixed oxide materials showed a humble fluorescence development at high potentials versus SHE leading to a position in the low activity area at the top right corner (marked with black cycles) of the $E(F_{50})/E_{Onset}$ versus SHE [V] plane in Figure 4 and were thus excluded from further validation and material development steps.

Validation of the High-Throughput Results of Noble-Metal Free Materials and Further Material Development Steps. Validation of the screening results was achieved by single-material fluorescence-based measurements according to the high-throughput

dx.doi.org/10.1021/co2000967 |ACS Comb. Sci. 2011, 13, 518–529

Table 2. Lattice Parameters of MoO_2 (tugarinovite)[30] and the Cu-Containing MoO_2 Phase in Cu_2Mo_{98}

		lattice parameters			
		a [Å]	*b* [Å]	*c* [Å]	*β* [deg]
absolute	MoO_2 (Tugarinovite)[30]	5.6096(2)	4.8570(2)	5.6259(22)	120.912(2)
	Cu_2Mo_{98}	5.606(3)	4.843(2)	5.6169(3)	120.921(1)
relative	MoO_2 (Tugarinovite)/Cu_2Mo_{98}	1.001	1.003	1.002	0.999

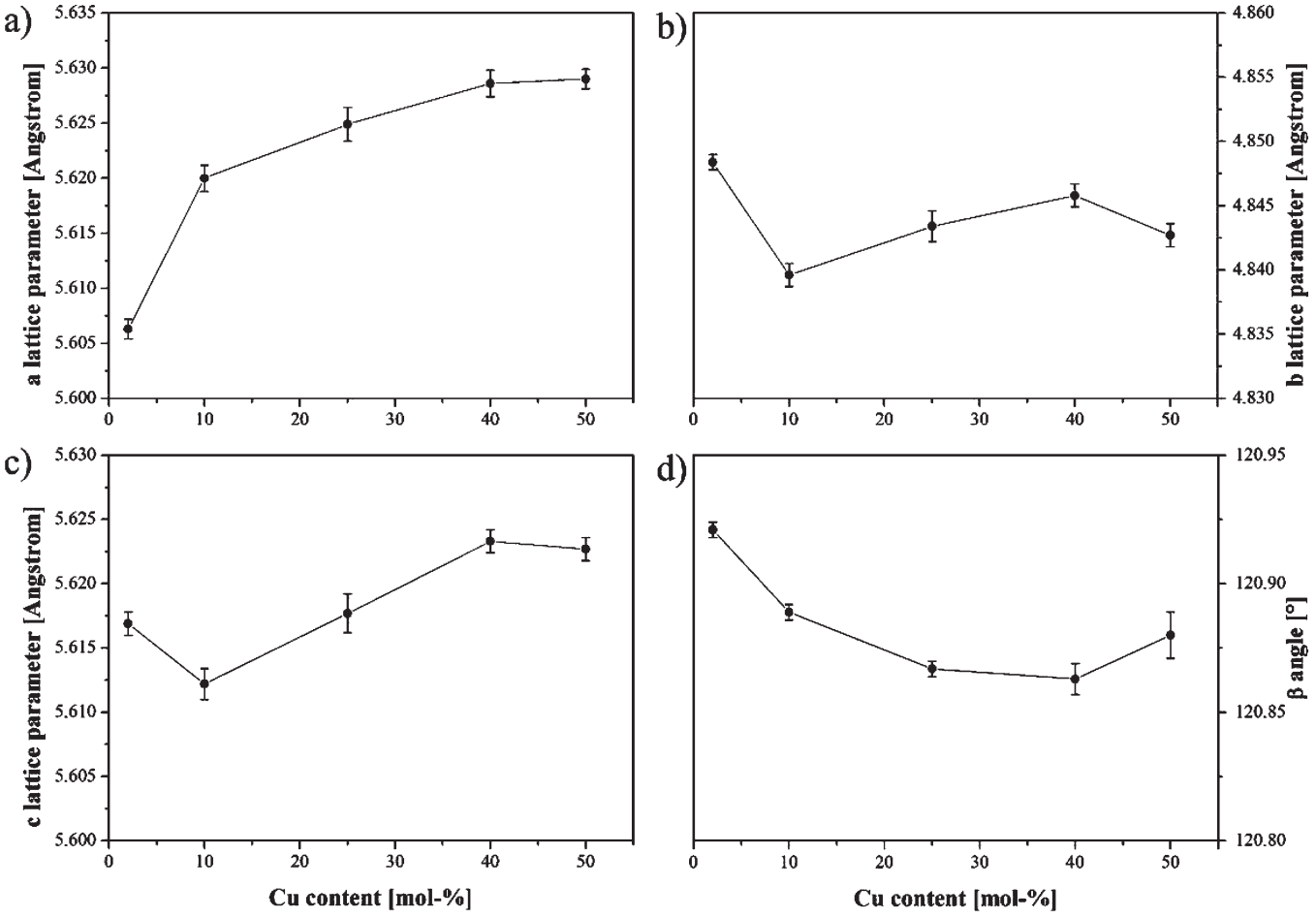

Figure 5. Change of the lattice parameters *a* (a), *b* (b), *c* (c), and *β* (d) in dependence of the Cu content in the $Cu_xMo_{1-x}O_x$ compounds (error bars $\pm 3\sigma$).

screening parameters with enhancement of data quality by the additional use of glass frits as diffusion barriers for the fluorescent dye as described before (see also Supporting Information, Figure S1).[10] The high throughput fluorescence results were confirmed by validation experiments. In comparison to the HT results only Cu_2Mo_{98} showed a small shift to lower E_{Onset} values comparable to PtRu as a result of the use of glass frits. As a result of a decrease in the E_{Onset} and $E(F_{50})$ values combined with an increase of the F_{50} value, $Cu_{25}Mo_{75}$, FeMoTa, and FeMoTi showed a shift closer to PtRu (see also Supporting Information, Figure S2). The validation experiments allowed to select Cu_2Mo_{98} as the material with the lowest E_{Onset} and $E(F_{50})$ value and a F_{50} value comparable to PtRu.

For further material developing steps, the binary Cu−Mo system (2nd generation) was chosen as a lead system. To determine the binary material with the highest fluorescence development, the composition variations $Cu_{10}Mo_{90}$, $Cu_{40}Mo_{60}$, and $Cu_{50}Mo_{50}$ were synthesized. $Cu_{50}Mo_{50}$ had been determined as the limit for acid stable binary Cu and Mo containing mixed oxides in former acid stability tests. Highest activity was obtained with the oxides of low Cu content. The measurements were conducted with and without the addition of methanol to the electrolyte as control experiments. In contrast to PtRu the binary Cu and Mo containing catalysts showed significant fluorescence development also in the absence of methanol. Cu_2Mo_{98} showed the second lowest E_{Onset} and the highest F_{50} value. $Cu_{10}Mo_{90}$ showed the lowest E_{Onset} value in the presence of methanol (results are summarized in Supporting Information, Figure S3).

Considering the measurements in a methanol-free electrolyte, for Cu_2Mo_{98} in comparison to $Cu_{10}Mo_{90}$ a faster decrease in the F_{50} value and a more distinctive shift to higher $E(F_{50})$ values was observed. This indicates for Cu_2Mo_{98} a stronger fluorescence

dx.doi.org/10.1021/co2000967 |ACS Comb. Sci. 2011, 13, 518–529

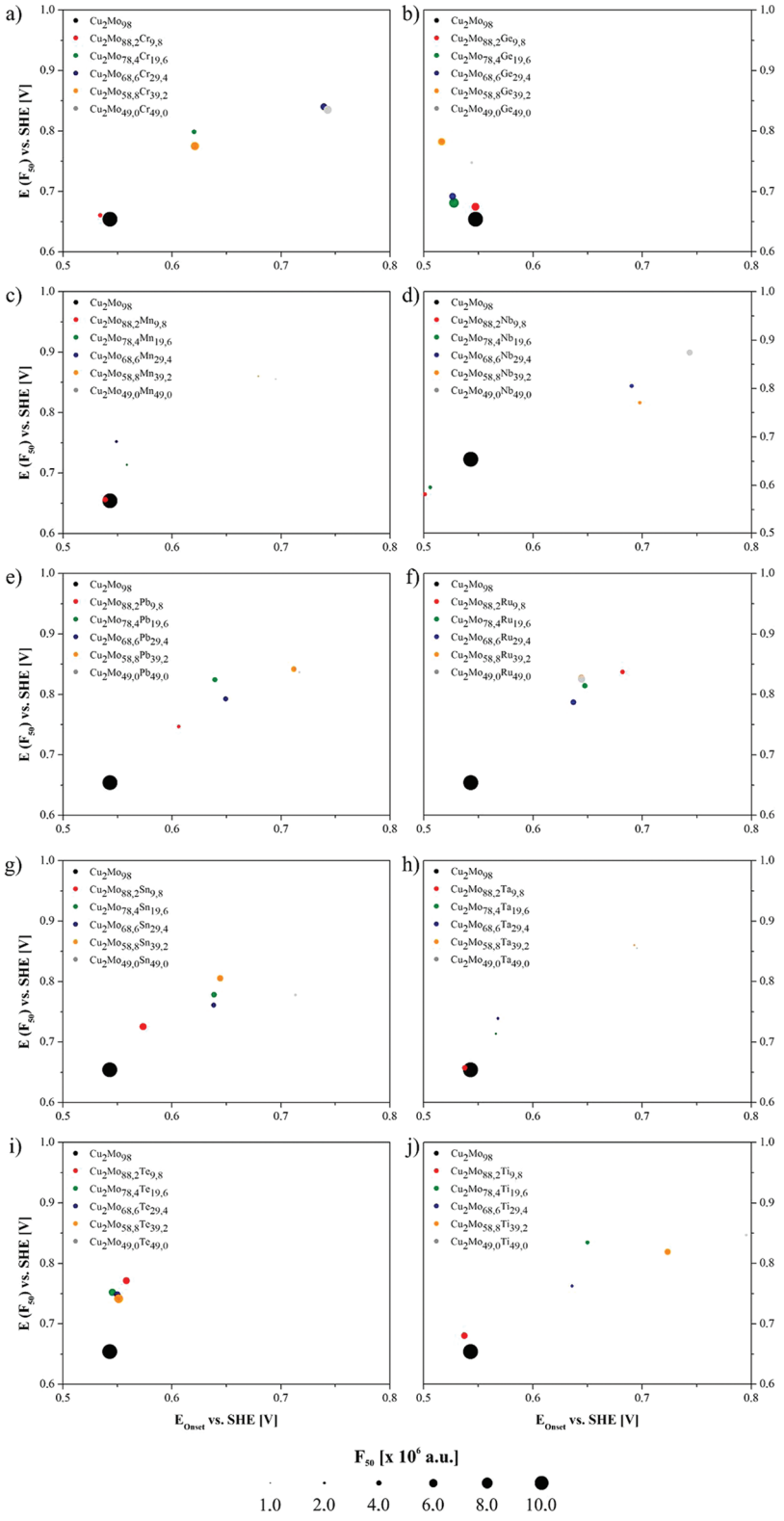

Figure 6. Comparison of the fluorescence development of compounds $Cu_2Mo_{(98-a)}X_a$ with a = 10, 20, 30, 40, and 50 mol % of the Mo content in Cu_2Mo_{98} and X = (a) Cr, (b) Ge, (c) Mn, (d) Nb, (e) Pb, (f) Ru, (g) Sn, (h) Ta, (i) Te, and (j) Ti by means of their position in the $E(F_{50})/E_{Onset}$ plane and the fluorescence intensity F_{50}, reference material: Cu_2Mo_{98}, axis caption line by line and column by column, respectively.

and thus higher activity because of the methanol oxidation than for the other Cu−Mo containing materials. ICP-MS analysis of the electrolyte after the measurement with Cu_2Mo_{98} showed a stoichiometric ratio of Cu and Mo indicating a dissolution of the compounds during the potential increase and thus pointing to additional fluorescence forming reactions competitive to the

dx.doi.org/10.1021/co2000967 |*ACS Comb. Sci.* 2011, 13, 518–529

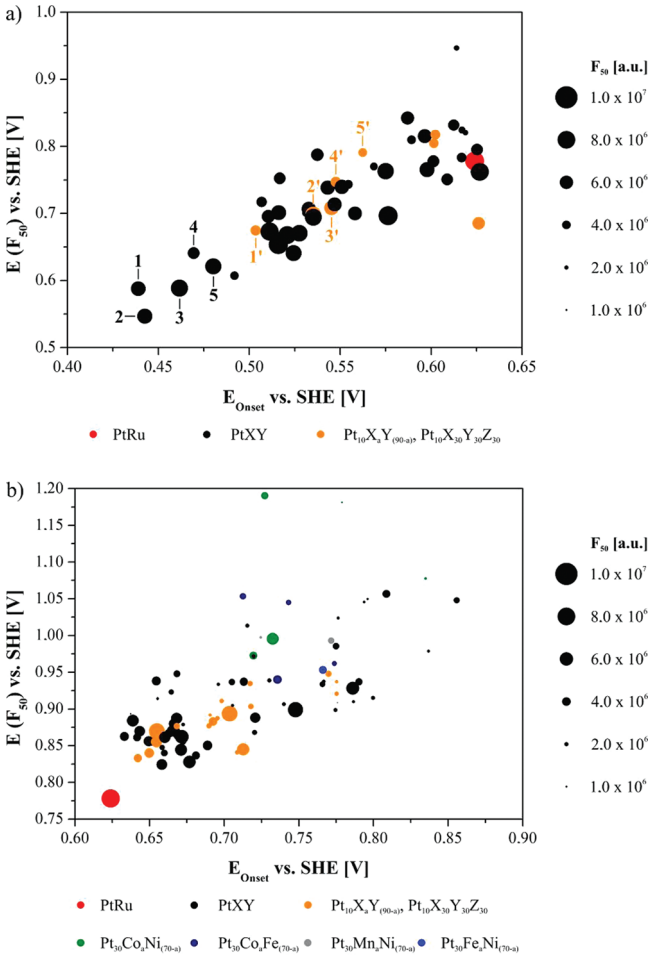

Figure 7. Comparison of the Pt containing materials activity toward the electro oxidation of methanol obtained in the high throughput screening by means of their position in the $E(F_{50})/E_{Onset}$ plane and the fluorescence intensity F_{50}, E_{Onset} value smaller (a) and larger (b) than 0.630 V versus SHE; for numeration of materials see text.

methanol oxidation and to instability of the electrocatalysts under electrochemical conditions.

Cu_2Mo_{98}, $Cu_{10}Mo_{90}$, $Cu_{25}Mo_{75}$, $Cu_{40}Mo_{60}$, and $Cu_{50}Mo_{50}$ have been investigated by XRD pattern (see also Supporting Information, Figure S4). According to the Cu−Mo binary phase diagram[28] no intermetallic Cu−Mo phases exist and accordingly by the reduction of mixed oxides at 450 °C in H_2 no intermetallic phases were observed. The reflections obtained for Cu_2Mo_{98} and their full width at half-maximum (fwhm) indicated the presence of MoO_2 (tugarinovite) as a well-crystalline phase in all samples. Even at 2 mol % Cu, but more significantly at larger Cu contents, a metallic fcc Cu phase grows in intensity with Cu content and with Cu contents higher than 40 mol % the reoxidation phases CuO (tenorite) and Cu_2O (cuprite) have to be included in the refinement model. Refinement of the lattice parameters (Table 2) of the monoclinic distorted rutile structure model of tugarinovite revealed data shown in Figure 5. As literature data on MoO_2 as reference differ significantly, they were purposely omitted in Figure 5. But even without the reference data for undoped tugarinovite, the data clearly indicate substitution of Mo by Cu in the cation sublattice. This effect is most pronounced for the length of the *a* axis and saturates not before 40 and 50 mol % nominal Cu content (Figure 5.a). In the monoclinic distorted rutile structure model of tugarinovite, the *a* axis just corresponds to the direction of the corner-sharing MoO_6 octahedra with the metallic interaction of the Mo^{4+} ions. By the substitution of Mo by Cu the degree of disturbance of this interaction and thus the lattice parameter change is highest compared to the other lattice parameters. From the simultaneous presence of other Cu phases in the Cu-doped MoO_2 samples it is clear that the degree of substitution is well below the nominal composition given as $Cu_xMo_{1-x}O_{2-x}$ ($0 \leq x \leq 0.5$). Without references the exact degree of substitution can not be specified.

Polymorphous MoO_2 crystallizes in distorted and undistorted variants of the tetragonal rutile structure like the oxides of the tetravalent ions of Cr, Ge, Mn, Nb, Pb, Ru, Sn, Ta, Te, and Ti, which were used as additives to the Cu−Mo oxides with the goal to improve stability and activity.[29] Doping was attempted by the substitution of Mo in the mixed oxides of a = 10, 20, 30, 40, and 50 mol % to obtain the general composition $Cu_2Mo_{(98-a)}X_a$ (3rd generation). The XRD patterns of $Cu_2Mo_{88.2}X_{9.8}$ with X = Cr, Ge, Mn, Nb, Pb, Ru, and Sn have been obtained and can be inspected in the Supporting Information, Figure S5. Except in the case of the addition of Ru, which formed a material of amorphous character, in all cases crystalline MoO_2 phases were identified.

Figure 6 shows the results of the fluorescence based activity measurements of the 50 doped Cu_2Mo_{98} materials by means of their relative position in the $E(F_{50})/E_{Onset}$ versus SHE [V] plane in comparison to the reference material Cu_2Mo_{98}. With increasing Mo substitution X in general, a shift of E_{Onset} and $E(F_{50})$ values to higher potentials combined with a decrease of F_{50} values was observed. The same dependency of the relative activity values on the Mo content and therefore the content of the crystalline Cu containing MoO_2 phase showed the compounds Cu_2Mo_{98}, $Cu_{10}Mo_{90}$, $Cu_{40}Mo_{60}$, and $Cu_{50}Mo_{50}$ (not shown). Only Mo substitution with Ge, Te, and Ru did not follow this general trend. The addition of Ge led to a decrease of the F_{50} values with a marginal shift of the E_{Onset} value to lower potentials combined with a shift of the $E(F_{50})$ value to higher potentials with increasing Ge content. A similar shift of the E_{Onset} and $E(F_{50})$ values was observed by Mo substitution with Te and Ru. An increase in the Te dopant concentration led to a minor effect on the E_{Onset} values accompanied by a shift to increased $E(F_{50})$ values and a uniform decrease of the F_{50} values. In contrast the Ru addition led to a distinct shift of the E_{Onset} values to higher potentials. Overall the reduced electrocatalytic activities of the $Cu_2Mo_{(98-a)}X_a$ compounds in comparison to the undoped Cu_2Mo_{98} and the reference catalyst PtRu did not provide new promising leads. Because of the poor electrostability of the Cu−Mo catalysts and the lack of additional promising leads, the search for noble-metal free mixed oxide electrocatalysts was terminated and the project focus was turned to electrocatalysts of low noble metal content. The focus of this contribution has been the discovery of new, stable electrocatalysts for the methanol oxidation reaction as alternatives to Pt−Ru. The best systems found and described above show good activity, but no stability. Their activity might result from a dissolution of at least one component of the mixtures as ICP analyses revealed molybdate ions in the electrolyte solutions after cycling. Thus we felt, that as long as the stability can not be improved, further studies with these materials are not justified.

High-Throughput Screening of Pt-Containing Materials. All the Pt containing mixed oxides were synthesized by similar sol−gel procedures as already used for the synthesis of the mixed

dx.doi.org/10.1021/co2000967 |*ACS Comb. Sci.* 2011, 13, 518–529

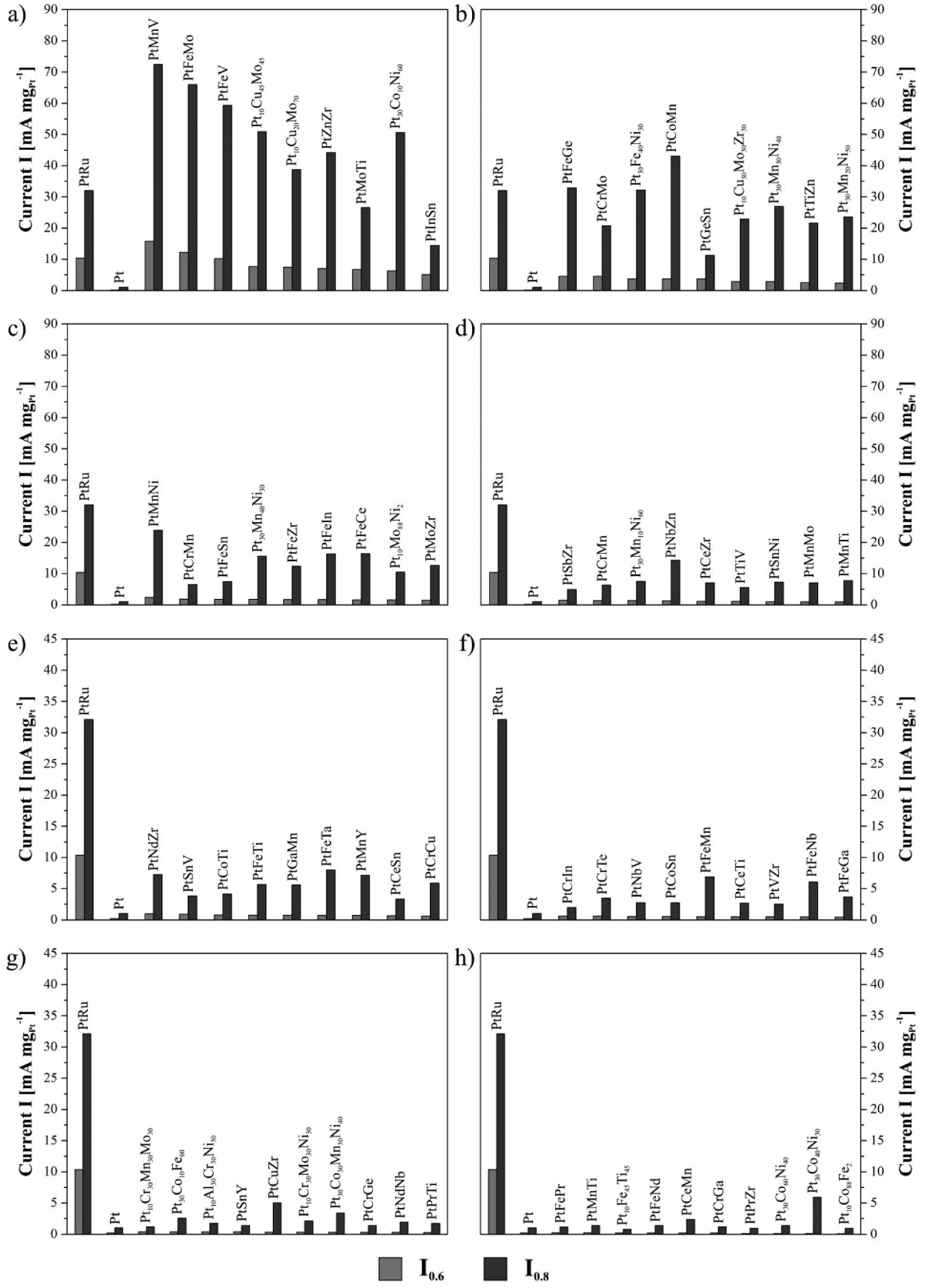

Figure 8. Comparative values $I_{0.6}$ and $I_{0.8}$ (out of the 20th forward scan) of the materials validated in CV experiments identified in high-throughput experiments according to a decreasing $I_{0.6}$ value (a−h).

dx.doi.org/10.1021/co2000967 |*ACS Comb. Sci.* 2011, 13, 518–529

oxides described above. Here the objective was to identify materials of high electrocatalytic activity for MeOH oxidation with a low Pt content. On the basis of the results of the noble-metal free screening, only hydrogen pretreated materials were considered in the following development steps. The design of experiment (DoE) of the Pt containing materials was based on the results from the screening of the other mixed oxides. First all the acid stable hydrogen treated materials identified in the former acid stability screening were doped with a Pt content of 10 mol % according to the formula $Pt_{10}X_aY_{(90-a)}$. Considering the low number of ternary Pt containing catalysts[10] and their potential importance as lead compounds in a generic development process for multinary catalysts, ternary compositions PtXY were synthesized. Thereby, the element X is forming an acid stable oxide (Cr, Fe, Mn, Nb, Sn, Ta, Ti, Zr)[30] and element Y was one of the elements Bi, Co, Ce, Cu, Ga, Ge, In, La, Mo, Nd, Ni, Pr, Sb, Te, V, and Zn. In addition, the spectrum of potential catalysts was extended by the synthesis of materials with the general composition $Pt_{30}X_aY_{(70-a)}$ with a = 10, 20, 30, 40, 50, and 60 mol % and XY = MnNi, FeMn, FeNi, CoFe, and CoNi.

Table 3. Materials Chosen for CV and XRD Based Stability Experiments with the Corresponding $I_{0.6}$ and $I_{0.8}$ Values for Activity Comparison

	$I_{0.6}$ [mA $(mg_{Pt})^{-1}$]	$I_{0.8}$ [mA $(mg_{Pt})^{-1}$]
PtMnV	15.83	72.46
PtFeMo	12.22	65.96
PtFeV	10.22	59.34
$Pt_{10}Cu_{45}Mo_{45}$	7.73	50.95
$Pt_{30}Co_{10}Ni_{60}$	6.35	50.65
PtZnZr	7.10	44.23
$Pt_{10}Cu_{20}Mo_{70}$	7.45	38.78
PtFeGe	4.53	32.93
$Pt_{30}Fe_{40}Ni_{30}$	3.80	32.22
$Pt_{30}Mn_{30}Ni_{40}$	2.88	26.98
$Pt_{30}Mn_{20}Ni_{50}$	2.41	23.61
$Pt_{10}Cu_{30}Mo_{30}Zr_{30}$	2.93	22.92
PtTiZn	2.60	21.66
PtCrMo	4.52	20.78
PtRu	10.37	32.11
Pt	0.21	1.05

From the 318 synthesized compounds 142 materials showed an increase in the fluorescence intensity at the applied potential range between 0.300 and 1.175 V versus SHE. Figure 7 compares the activity of the materials toward the electrooxidation of methanol by means of their relative position to PtRu in the $E(F_{50})/E_{Onset}$ versus SHE [V] plane including the half fluorescence value F_{50}. For 44 members of the PtXY type materials (33 mol % of each element) and 8 materials of the $Pt_{10}X_aY_{(90-a)}$ type a lower fluorescence intensity onset potential E_{Onset} than for PtRu was obtained (Figure 7a). The lowest E_{Onset} values in combination with the lowest fluorescence intensity F_{50} in comparison to PtRu were achieved from the elemental combinations PtCrMo (1), PtFeMo (2), PtCrGe (3), PtVZr (4), and PtMnTa (5). In case of the $Pt_{10}X_aY_{(90-a)}$ type materials $Pt_{10}Al_{30}Mo_{30}Nb_{30}$ (1′), $Pt_{10}Mo_{30}Cr_{30}Ni_{30}$ (2′), $Pt_{10}Fe_{30}Mo_{30}Ti_{30}$ (3′), $Pt_{10}Fe_{45}Ti_{45}$ (4′), and $Pt_{10}Cu_{30}Ti_{30}Zr_{30}$ (5′) exhibited the lowest fluorescence intensity onset potentials E_{Onset} with a half fluorescence intensity potential $E(F_{50})$ lower than PtRu. Corresponding to a lower methanol conversion, these materials showed a lower fluorescence intensity F_{50} than the PtXY type materials mentioned before and PtRu (Figure 7a). In the case of the $Pt_{30}X_aY_{(70-a)}$ type materials only the XY combinations of the elements Mn Ni, Fe Ni, Co Fe, and Co Ni showed a change in the fluorescence value during the measurement. The fluorescence onset potentials E_{Onset} were located in the range of 0.70 and 0.80 V versus SHE (Figure 7b). In combination with the low half fluorescence intensities F_{50} and the high half fluorescence intensity potentials $E(F_{50})$ compared to the reference material PtRu, a minor activity of the $Pt_{30}X_aY_{(70-a)}$ type materials toward the electrooxidation of methanol was observed.

Validation of the Methanol Electrooxidation Activity of Pt Containing Materials Identified in High-Throughput Screening and Stability Test of Selected Materials. The

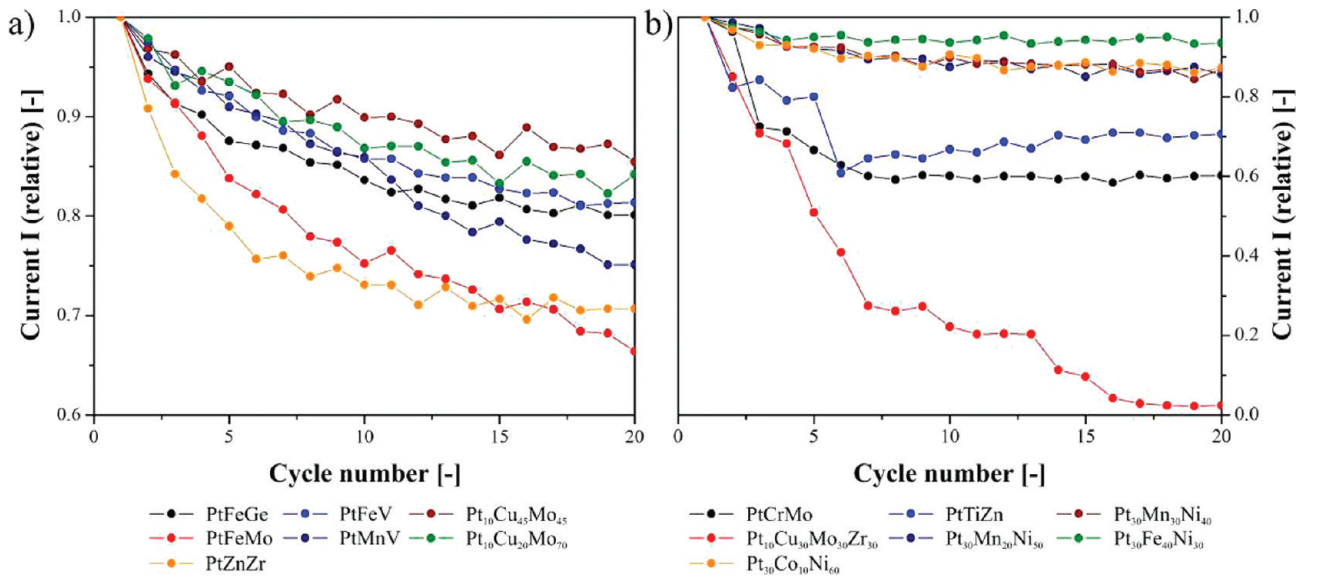

Figure 9. Dependence of the currents at 1.050 V versus SHE from the cycle number obtained in the CV experiment normalized to the current obtained at the 1st forward scan.

dx.doi.org/10.1021/co2000967 |ACS Comb. Sci. 2011, 13, 518–529

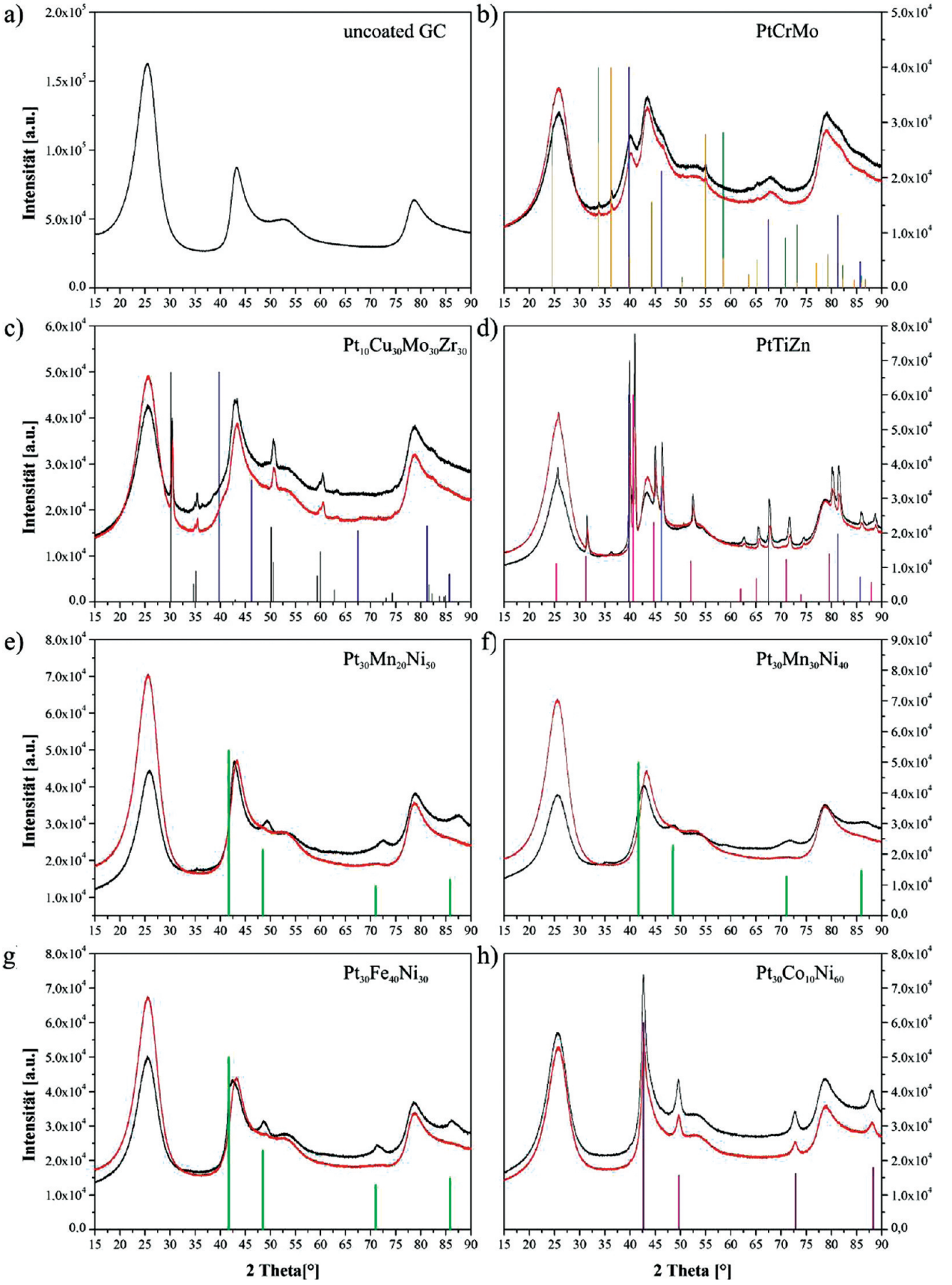

Figure 10. XRD pattern of (a) uncoated glassy carbon plate, (b) PtCrMo, (c) $Pt_{10}Cu_{30}Mo_{30}Zr_{30}$, (d) PtTiZn, (e) $Pt_{30}Mn_{20}Ni_{50}$, (f) $Pt_{30}Mn_{30}Ni_{40}$, (g) $Pt_{30}Fe_{40}Ni_{30}$, (h) $Pt_{30}Co_{10}Ni_{60}$ before (black) and after the CV experiments (red); reference line patterns were given only for identified phases after the stability experiments.

dx.doi.org/10.1021/co2000967 |*ACS Comb. Sci.* 2011, 13, 518–529

validation of the activity of the materials identified in high-throughput experiments was carried out in a conventional CV setup in 0.5 M H_2SO_4 solution containing 1 M methanol after a cycling in pure 0.5 M H_2SO_4 solution. For comparison of the methanol electrooxidation activity the currents at 0.60 V versus SHE ($I_{0.6}$) and 0.80 V versus SHE ($I_{0.8}$) normalized to the Pt content in each material were taken from the methanol oxidation current curves measured in the 20th forward scan of each CV experiment. The two values were indicating the activity of the materials at low and high anode potentials. Figure 8 summarizes the $I_{0.6}$ and $I_{0.8}$ values of the 74 materials with currents larger than 1 mA $(mg_{Pt})^{-1}$. In case of the PtXY type materials PtMnV, PtFeMo, and PtFeV higher $I_{0.6}$-values and twice as high $I_{0.8}$-values compared to PtRu were obtained. Assuming a correlation of these values with the electrooxidation activity, this observation is indicative of a higher methanol electrooxidation activity than for PtRu. For PtFeGe, PtCrMo, and the $Pt_{30}X_aY_{(70-a)}$ type material $Pt_{30}Fe_{40}Ni_{30}$ $I_{0.6}$ values half as high as the value for PtRu and $I_{0.8}$ values larger than 60% of the value for PtRu were obtained. For all the materials given in Figure 8 a–h higher $I_{0.6}$ and $I_{0.8}$ values than for Pt were determined. Table 3 shows the materials chosen for the stability test.

The stability tests were performed in a CV setup. After cycling of the electrode catalyst in 0.5 M H_2SO_4 the methanol oxidation current at 1.050 V in each of the 20 forward scans was used as stability criteria. In contrast to the validation experiments, glassy carbon plates as carrier for the electrode preparation were used instead of graphite disks which allowed XRD analysis of the electrode preparations before and after the CV experiments.

Figure 9 shows the dependence of the currents at 1.050 V versus SHE from the cycle number obtained in the CV experiments normalized to the current obtained at the first forward scan of the materials given in Table 3. The relative current characteristics of PtFeGe, PtFeV, $Pt_{10}Cu_{45}Mo_{45}$, and $Pt_{10}Cu_{20}Mo_{70}$ (Figure 9 a) showed a tendency to stabilize between the 15th and 17th cycle, whereas the relative current characteristics of PtMnV and PtFeMo showed a constant decrease over 20 cycles. In contrast to this, the relative current characteristics of PtZnZr showed a stabilization of the current signal after a severe decrease in the first 10 cycles of the experiment. After a decrease within the first three cycles to 90% of the starting current, the relative currents of $Pt_{30}Mn_{30}Ni_{40}$, $Pt_{30}Mn_{30}Ni_{50}$, $Pt_{30}Fe_{30}Ni_{40}$ stabilized (Figure 9 b). Only the relative current of $Pt_{10}Cu_{30}Mo_{30}Zr_{30}$ decreased to 5% of the starting value. Decreases of the relative currents were attributed to partial dissolutions of the electrode catalysts. In case of a current stabilization, the presence of a stable and active catalyst was assumed.

Under the aspect of the presence of crystalline phases before and after the CV experiments in methanol-free and methanol containing H_2SO_4 solution, the electrode preparations were analyzed by XRD methods. The XRD pattern of the materials given in Figure 9 a and b were used as indicators of material stability as they suggest that the decreases in the relative currents are caused by a dissolution of crystalline components. The materials associated with Figure 9a are given in Supporting Information, Figure S6, and the materials associated with Figure 9b are shown in Figure 10. In the case of PtFeGe, PtFeV, $Pt_{10}Cu_{45}Mo_{45}$, and $Pt_{10}Cu_{20}Mo_{70}$ the formation of a constant current resulted apparently from the stability of a Pt containing phase active for the electrooxidation of methanol and the complete dissolution of all other crystalline components. In the case of PtZnZr the constant relative current resulted from the phases Pt, PtZn, and ZrO_2. Similar to PtZnZr, the constant relative current of PtCrMo, PtTiZn, and $Pt_{30}Co_{10}Ni_{60}$ resulted from the presence of Pt containing phases. In $Pt_{30}Mn_{30}Ni_{40}$, $Pt_{30}Mn_{30}Ni_{50}$, and $Pt_{30}Fe_{30}Ni_{40}$ the identified PtNi phase disappeared during the CV experiments. In combination with the stable current (Figure 9 b) this points to an important role of amorphous parts in the materials for the methanol oxidation. For example PtFeNi displays excellent electrochemical stability (Figure 9b), while the microstructure has changed during the CV test (Figure 10). Obviously it has to be differentiated between electrochemical and structural stability. Electrochemically this composition is stable over more than 20 cycles, whereas its structural stability is not. The XRD pattern reveals amorphization during cycling, but as structure–activity relations are not known, the only conclusion drawn from these investigations is that the presence of oxide phases, such as ZrO_2 or Cr_2O_3 does not result in stable catalysts whereas the presence of alloy phases, such as PtMx seem to be a prerequisite for stability, whether (nano)crystalline or not. In this study the compositions PtTiZn, $Pt_{30}Co_{10}Ni_{60}$, $Pt_{30}Mn_{20}Ni_{50}$, $Pt_{30}Mn_{30}Ni_{40}$, and $Pt_{30}Fe_{40}Ni_{30}$ have been discovered as new leads, which have to be investigated in more detail.

4. SUMMARY

With the help of our fluorescence based high-throughput screening technology, a highly diverse search for alternative anode electrocatalysts has been conducted. The materials preparation was based on the sol–gel synthesis of mixed oxides, which were studied as prepared as well as after a H_2 pretreatment at 450 °C. The screening of 260 acid stable compounds, identified out of a range 1100 mixed oxides and hydrogen treated mixed oxides by an optical prescreening method, led to the identification of Cu and Mo containing materials as lead compounds for further development steps. Cu_2Mo_{98} was identified as material with Cu substituting Mo ions in the cation sublattice and the highest fluorescence development during the high-throughput screening. ICP-MS measurements of the methanol-containing and methanol-free electrolyte used for single material measurements resulted in a stoichiometric dissolution of the elements of the binary Cu–Mo composition spread. The attempt to stabilize the structure of the Cu containing MoO_2 phases in Cu_2Mo_{98} by the addition of Cr, Ge, Mn, Nb, Pb, Ru, Sn, Ta, Te, and Ti led to a decrease in fluorescence and hence a reduction of the catalytic activity for the electrooxidation of methanol. Despite the highly diverse search space of mixed oxides across the periodic table, no stable electrocatalyst of sufficient catalytic activity and stability could be found. Therefore the study was extended to Pt containing materials with the objective to provide catalysts of reduced Pt content and higher electrocatalytic activity compared to the reference PtRu. In the high-throughput screening of 318 materials with a Pt content of 10 mol % or 30 mol %, 142 materials showed a promising fluorescence development. Standard CV experiments validated the methanol oxidation activity of 74 materials. By stability tests based on CV and XRD analysis of the electrode preparation before and after the CV experiments. PtTiZn, $Pt_{30}Co_{10}Ni_{60}$, $Pt_{30}Mn_{20}Ni_{50}$, $Pt_{30}Mn_{30}Ni_{40}$, and $Pt_{30}Fe_{40}Ni_{30}$ were identified as lead compositions for further combinatorial material development steps, all of which indicate significant improvements of the electrocatalytic activity relative to PtRu.

■ ASSOCIATED CONTENT

Supporting Information. Several diagrams and schemes, provided for more detailed understanding of the arguments and conclusions presented. Figure S1 shows the frits used for conventional measurements and their positioning in the channels between the catalyst wells. Figure S2 shows the results of the validation experiments in comparison to those of the high-throughput experiments. The activity of the 10 materials is elucidated by means of their relative position in the $E(F_{50})/E_{Onset}$ versus SHE [V] plane including F_{50}. $Cu_{25}Mo_{75}$, FeMoTa, and FeMoTi showed a position shift to the lower left next to the position of PtRu as a result of a decrease in the E_{Onset} and $E(F_{50})$ values combined with an increase of the F_{50} value. Figure S3 displays the results of the fluorescence-based measurements for Cu_2Mo_{98}, $Cu_{10}Mo_{90}$, $Cu_{40}Mo_{60}$, $Cu_{50}Mo_{50}$, and the reference material PtRu. Figure S4 shows the XRD pattern for Cu_2Mo_{98}, $Cu_{10}Mo_{90}$, $Cu_{25}Mo_{75}$, $Cu_{40}Mo_{60}$, and $Cu_{50}Mo_{50}$. The XRD pattern of $Cu_2Mo_{88.2}X_{9.8}$ with X = Cr, Ge, Mn, Nb, Pb, Ru, and Sn are given in Figure S5. In Figure S6 the XRD of uncoated glassy carbon iscompared with the XRDs of PtFeGe, PtFeMo, PtFeV, PtMnV, $Pt_{10}Cu_{45}Mo_{45}$, $Pt_{10}Cu_{20}Mo_{70}$ and PtZnZr (materials of Figure 9a). This material is available free of charge via the Internet at http://pubs.acs.org.

■ AUTHOR INFORMATION

Corresponding Author

*Phone: +496 81 302 2422. E-mail: w.f.maier@mx.uni-saarland.de.

Funding Sources

The authors thank Umicore AG for support.

■ ACKNOWLEDGMENT

The authors thank M. Duisberg, M. Lopez, M. Daurer, and D. Herein from Umicore AG for discussions. The authors also thank C. Möser and R. Kautenburger from Saarland University for the ICP-MS measurements.

■ REFERENCES

(1) Mauritz, K. A.; Moore, R. B. State of understanding of Nafion. *Chem. Rev.* **2004**, *104*, 4535–4585.

(2) Hamnett, A. Mechanism and electrocatalysis in the direct methanol fuel cell. *Catal. Today* **1997**, *38*, 445–457.

(3) Hogarth, M. P.; Hards, G. A. Direct methanol fuel cells. Technological advances and further requirements. *Platinum Met. Rev.* **1996**, *40*, 150–159.

(4) Huang, J. C.; Liu, Z. L.; He, C. B.; Gan, L. M. Synthesis of PtRu nanoparticles from the hydrosilylation reaction and application as catalyst for direct methanol fuel cell. *J. Phys. Chem. B* **2005**, *109*, 16644–166649.

(5) Chan, B. C.; Liu, R. X.; Jambunathan, K.; Zhang, H.; Chen, G. Y.; Mallouk, T. E.; Smotkin, E. S. Comparison of high-throughput electrochemical methods for testing direct methanol fuel cell anode electrocatalysts. *J. Electrochem. Soc.* **2005**, *152*, A594–A600.

(6) Hogarth, M. P.; Ralph, T. R. Catalysis for low temperature fuel cells: Part III: Challenges for the direct methanol fuel cell. *Platinum Met. Rev.* **2002**, *46*, 146–164.

(7) Wang, Z. B.; Yin, G. P.; Shi, P. F. Stable Pt-Ru/C catalysts prepared from new precursors by thermal reduction for direct methanol fuel cell. *J. Electrochem. Soc.* **2005**, *152*, A2406–A2412.

(8) Wu, B. H.; Hu, D.; Kuang, Y. J.; Liu, B.; Zhang, X. H.; Chen, J. H. Functionalization of Carbon Nanotubes by an Ionic-Liquid Polymer: Dispersion of Pt and PtRu Nanoparticles on Carbon Nanotubes and Their Electrocatalytic Oxidation of Methanol. *Angew. Chem., Int. Ed.* **2009**, *48*, 4751–4754.

(9) Loffler, M. S.; Natter, H.; Hempelmann, R.; Wippermann, K. Preparation and characterization of Pt-Ru model electrodes for the direct methanol fuel cell. *Electrochim. Acta* **2003**, *48*, 3047–3051.

(10) Welsch, F. G.; Stöwe, K.; Maier, W. F. Rapid optical screening technology for direct methanol fuel cell (DMFC) anode and related electrocatalysts. *Catal. Today* **2011**, *159*, 108–119.

(11) Manohara, R.; Goodenough, J. B. J. Methanol Oxidation in Acid on Ordered NiTi. *Mater. Chem.* **1992**, *2*, 875–887.

(12) Liu, H.; Zhang, J. *Electrocatalysis of Direct Methanol Fuel Cells*; Wiley-VCH: Weinheim, Germany, 2009.

(13) Strasser, P. Combinatorial optimization of ternary Pt alloy catalysts for the electrooxidation of methanol. *J. Comb. Chem.* **2008**, *10*, 216–224.

(14) Smotkin, E. S.; Jiang, J. H.; Nayar, A.; Liu, R. X. High-throughput screening of fuel cell electrocatalysts. *Appl. Surf. Sci.* **2006**, *252*, 2573–2579.

(15) Jiang, R. Z.; Rong, C.; Chu, D. Combinatorial approach toward high-throughput analysis of direct methanol fuel cells. *J. Comb. Chem.* **2005**, *7*, 272–278.

(16) Brace, K. M.; Hayden, B. E.; Russell, A. E.; Owen, J. R. A parallel optical screen for the rapid combinatorial electrochromic analysis of electrochemical materials. *Adv. Mater.* **2006**, *18*, 3253–3257.

(17) Reddington, E.; Sapienza, A.; Gurau, B.; Viswanathan, R.; Saragapani, S.; Smotkin, E. S.; Mallouk, T. E. Combinatorial Electrochemistry: A Highly Parallel, Optical Screening Method for Discovery of Better Electrocatalysts. *Science* **1998**, *280*, 1735–1737.

(18) Chu, Y. H.; Ahn, S. W.; Kim, D. Y.; Kim, H. J.; Shul, Y. G.; Han, H. S. Combinatorial investigation of Pt-Ru-M as anode electrocatalyst for direct methanol fuel cell. *Catal. Today* **2006**, *111*, 176–181.

(19) Prochaska, M.; Jin, J.; Rochefort, D.; Zhuang, L.; DiSalvo, F. J.; Abruna, H. D.; van Dover, R. B. High throughput screening of electrocatalysts for fuel cell applications. *Rev. Sci. Instrum.* **2006**, *77*, 054104 1–8.

(20) Choi, W. C.; Kim, J. D.; Woo, S. I. Quaternary Pt-based electrocatalyst for methanol oxidation by combinatorial electrochemistry. *Catal. Today* **2002**, *74*, 235–240.

(21) Jin, J.; Prochaska, M.; Rochefort, D.; Kim, D. K.; Zhuang, L.; DiSalvo, F. J.; van Dover, R. B.; Abruna, H. D. A high-throughput search for direct methanol fuel cell anode electrocatalysts of type $Pt_xBi_yPb_z$. *Appl. Surf. Sci.* **2007**, *254*, 653–661.

(22) Gregoire, J. M.; Kostylev, M.; Tague, M. E.; Mutolo, P. F.; van Dover, R. B.; DiSalvo, F. J.; Abruna, H. D. High-Throughput Evaluation of Dealloyed Pt-Zn Composition-Spread Thin Film for Methanol-Oxidation Catalysis. *J. Electrochem. Soc.* **2009**, *156*, B160–B166.

(23) Frenzer, G.; Maier, W. F. Amorphous porous mixed oxides: Sol-gel ways to a highly versatile class of materials and catalysts. *Ann. Rev. Mater. Res.* **2006**, *36*, 281–331.

(24) Shimooka, H.; Kuwabara, M. Preparation of Dense $BaTio_3$ Ceramics from Sol-Gel-Derived Monolithic Gels. *J. Am. Ceram. Soc.* **1995**, *78*, 2849–2852.

(25) Shimooka, H.; Kuwabara, M. Crystallinity and stoichiometry of nano-structured sol-gel-derived $BaTiO_3$ monolithic gels. *J. Am. Ceram. Soc.* **1996**, *79*, 2983–2985.

(26) Shimooka, H.; Kohiki, S.; Kobayashi, T.; Kuwabara, M. Preparation of translucent barium titanate ceramics from sol-gel-derived transparent monolithic gels. *J. Mater. Chem.* **2000**, *10*, 1511–1512.

(27) Scheidtmann, J.; Saalfrank, J. W.; Maier, W. F. Plattenbau-automated synthesis of catalysts and materials libraries. *Stud. Surf. Sci. Catal.* **2003**, *145*, 13–20.

(28) Subramanian, P. R.; Laughlin, D. E. The Cu-Mo (copper-molybdenum) system. *Bull. Alloy Phase Diagrams* **1990**, *11*, 169–172.

(29) Wyckhoff, R. W. G. *Crystal Structures*, 2nd ed.; Wiley & Sons: New York, 1963.

(30) Hollemann, A. F.; Wiberg, N. *Lehrbuch der Anorganischen Chemie*; Walter de Gruyter: Berlin, Germany, 1995.